Macromolecules

ARTICLE

pubs.acs.org/Macromolecules

A New Scenario of Shish-Kebab Formation from Homogeneous Solutions of Entangled Polymers: Visualization of Structure Evolution along the Fiber Spinning Line

Hiroki Murase,[†,‡,*] Yasuo Ohta,[†,‡] and Takeji Hashimoto[*,†,§,⊥]

[†]Department of Polymer Chemistry, Graduate School of Engineering, Kyoto University, Katsura, Nishikyo-ku, Kyoto 615-8510, Japan

[‡]Research Center, TOYOBO Co., Ltd., 2-1-1 Katata, Ohtsu-shi, Shiga 520-0292, Japan

ABSTRACT: Self-assembly of ordered structures under the external fields is one of the most important and fundamental research themes in physical science of soft matters including polymers. The "shish-kebab" self-assembly is a most intriguing but fundamental crystalline superstructure formed in polymers under various flow fields. Nevertheless the mechanism of shish-kebab formation is not fully understood yet. In order to clarify the mechanisms for polymer solutions, we have investigated the flow-induced self-assembling structures evolved along a fiber spinning line for concentrated polymer solutions and proposed a new scenario of the kinetic pathway leading to shish-kebab formation and various transient structures evolved therein. The proposed pathway comprises two stages: (i) the early stage pathway before an onset of the birefringence upturn, where the flow-induced phase separation plays a dominant role on creating a series of various transient structures leading to the "sring-like structure" (denoted as "string"), all of which are hardly able to be detected by conventional SAXS, SANS, and WAXD; (ii) the late stage pathway after the onset of the birefringence upturn where the flow-induced crystallization plays a dominant role on generating bundles of stretched chains, probably via the so-called coil−stretched chain transition, within the strings grown in the early stage pathway, followed by nucleation−growth of shishs and epitaxial crystallization of kebab lamellae onto shishs from the random coils incorporated within the demixed domains which coexist with shishs within the given string. Our work therefore elucidates an important role of the flow-induced phase separation on the flow-induced shish-kebab formation.

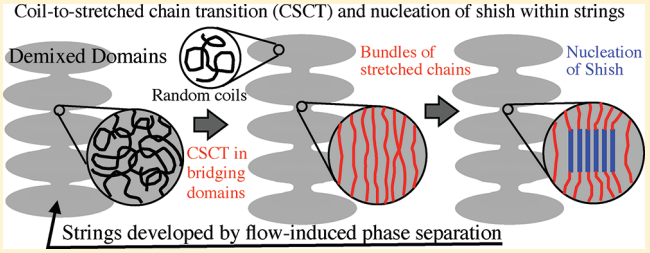

1. INTRODUCTION

The "shish-kebab" self-assembly is a most intriguing but fundamental crystalline superstructure formed in polymer solutions and melts under various flow fields such as shear flow, extensional flow, etc. Since the first discovery of shish-kebab structure formed in polymer solutions[1,2] about a half century ago, a great number of researchers have been attracted to this flow-induced superstructure and tried to elucidate its formation mechanism on the basis of the flow-induced crystallization phenomenon.[3−16] Nevertheless detailed kinetic pathways leading to shish-kebab formation have not yet been fully clarified. Furthermore, its investigation has now been one of the extremely hot research themes in polymer science. We also have been investigating the kinetic pathway as one of general research themes which belong to open nonequilibrium phenomena.[17−20] We have recently reported a short communication[21] about the kinetic pathway of shish-kebab formation from solutions of entangled polymers under shear flow and a flow field involved in a fiber spinning process. In this paper, we would like to present a full account of the kinetic pathway found in the fiber spinning process. We would like to first stress that the solutions of entangled polymers to be investigated here are thermodynamically stable single phase-solutions; hence, neither crystallization nor phase separation being involved in the absence of external flow fields.

Many works have been reported on the real-time and *in situ* analyses of birefringence (Δn), small-angle X-ray and neutron scattering (SAXS and SANS, respectively), wide-angle X-ray diffraction (WAXD), optical microscope images (OM) to investigate the kinetic pathway. However most of the works done up to this moment have explored only the stage after signatures of the flow-induced crystallization appear, e.g., after an onset of a sharp increase of Δn and an appearance of remarkable SAXS, SANS, and WAXD patterns. Let us designate this stage which has been explored so far as a *late stage kinetic pathway*. Many works have overlooked the kinetic pathway which may exist before the crystallization process. Let us define this kinetic pathway as an *early stage kinetic pathway*. From a series of our works[17−19] of shear-induced structures on solutions of entangled noncrystallizable polymers, as will be briefly described below, we believe that the early stage kinetic pathway is crucial to unveil the mechanism and process of shish-kebab formation. Consequently we have focused on the exploration of the early stage kinetic pathway in this work as well as in the previous works.[20,21]

Received: April 16, 2011
Revised: July 14, 2011
Published: September 01, 2011

Why can the early stage pathway be important? We think it is because our system belongs to the so-called dynamically asymmetric systems in which the constituent components of the systems, solute polymer and solvent, have a large mobility difference. The stress-diffusion coupling inherent in the dynamically asymmetric systems causes the flow induced concentration fluctuations and liquid−liquid phase separation[17−26] regardless whether the slow component is crystallizable or noncrystallizable polymers. Thus, our systems involve in general two kinds of flow-induced phase transitions: phase separation (liquid−liquid phase transition) and crystallization (liquid−solid phase transition). Hence a coupling of them seems to be crucial to unveil the pathway from entangled coils swollen with solvents to the shish-kebabs. If the flow-induced crystallization occurs prior to the flow-induced phase separation in such a way that effects of the phase separation do not utterly play roles on the pathway, the traditional approach would suffice to solve the problem. However if the opposite is the case, the traditional approach would not suffice, and we must take into account roles of phase separation on the crystallization leading to the shish-kebab structure. Surprisingly, *the coupling effects* in the polymer solutions have been left almost unexplored up to now in this research field, except for the work by McHugh and co-workers[27] and by us.[20,21,28−30] This is probably because the flow-induced phase separation occurs prior to the crystallization (in the early stage kinetic pathway), and the flow-induced phase-separated structures can be observed only in situ, as they decay rapidly and hence can not be observed after the cessation of the flow. It is also because signatures of the flow-induced phase separation do not cause the increase of remarkable Δn and are discerned at the length scale much larger than that relevant to SAXS, SANS, and WAXD.

2. BACKGROUNDS AND MOTIVATIONS

2.1. Previous Studies of Shish-Kebab Formation. Keller for the first time pointed out that the coil-to-stretched chain transition (CSCT),[3] which was theoretically predicted by de Gennes,[31] plays an important role on the flow-induced crystallization of polymers into the shish-kebabs. He demonstrated an abrupt increase in Δn, indicative of an appearance of the fully extended chains above a critical strain rate in dilute solution under extensional flow. Stimulated by his work, many experimental[4−16] and simulation works[32−34] have been carried out in order to clarify the CSCT and subsequent shish-kebab formation. Many researchers have investigated polymer melts, especially binary melt blends of the same polymer species having high and low molecular weight[5,7,8,16] to elucidate the CSCT occurring in the sections of chains between the entanglements. Here we would like to address the following question: Whether do the CSCT and subsequent formation of bundles of stretched chains occur in uniform solutions or in phase-separated solutions under the flow fields. In the case of melts with a large molecular weight polydispersity or with a binary mixture of the same polymers having large and small average molecular weights, high molecular weight species act as "polymer", while low molecular weight species act as "solvent" for the flow-induced phase separation in the context of the dynamic asymmetry.[21]

2.2. Role of Flow-Induced Concentration Fluctuations and Phase Separation on Kinetic Pathway Leading to Shish-Kebab. When semidilute polymer solutions are subjected to shear flow with shear rate $\dot{\gamma}$ greater than a critical value, the solutions become turbid because of the liquid−liquid phase-separation or the enhancement of concentration fluctuations induced by the shear.[18,19,35−40] This intriguing phenomenon is explained theoretically as a consequence of the stress-diffusion coupling inherent in the dynamically asymmetric systems.[22−26] Polymer chains have mobility much smaller than solvent molecules so that the latter relaxes much faster than the former. As a consequence stress developed in the system under shear flow will be born only by polymer chains, the relaxation process of which will then cause the shear-induced phase separation for the following reason. When the shear rate $\dot{\gamma}$ is larger than the terminal rheological relaxation rate τ_w^{-1}, the excess elastic free energy built up in the solution by the deformation of the entangled polymer chains can not be relaxed by disentanglements but can be released only by squeezing solvent from regions rich in polymers, hence bearing larger stress, into regions poor in polymers. By this squeezing, swollen deformed network chains can be relaxed. This solvent squeezing process mediated by the elastic effects results in enhancement of concentration fluctuations and phase separation under shear flow against osmotic pressure.

The shear-induced concentration fluctuations and phase separation were first studied mainly by using noncrystallizable ultrahigh molecular weight atactic polystyrene (UHMWaPS) solutions with the chain entanglements which are homogeneous in quiescent state. Later we found the same phenomena for solutions of entangled crystallizable ultrahigh molecular weight polyethylene (UHMWPE) with paraffin as a solvent by using in situ measurement of Δn, small-angle light scattering (SALS), and optical microscopy.[28−30,41] It is strikingly interesting for us to find that both the noncrystallizable and crystallizable solutions commonly give the following results (i−iii): (i) shear-enhanced concentration fluctuations at $\dot{\gamma} > \tau_w^{-1}$ where τ_w is the longest rhelogical relaxation time; (ii) formation of string-like structures where centers-of-mass of phase-separated domains aligned along a row parallel to the flow direction at $\dot{\gamma} > \tau_e^{-1}$ where τ_e is the chain retraction time;[20,21,42] (iii) a sharp change of optical properties of the strings from a small Δn to a large Δn with a further increasing $\dot{\gamma}$. The change involving a sharp upturn of Δn implies formation of the bundles of the stretched chains interconnecting the demixed domains within the strings. In the case of the crystallizable solutions, the strong optical anisotropy does remain even after cessation of shear flow, because of existence of the solidification mechanism due to the crystallization, which provides an important piece of information to elucidate formation of a precursor structure of the shish-kebabs. On the other hand in the case of the noncrystallizable solutions, the strings with the strong optical anisotropy relax back to an optically isotropic homogeneous solutions, because of absence of the solidification mechanism as described above.

2.3. Objectives of This Work Motivated by the Previous Results. Figure 1 highlights our objectives in this work (part A) in conjunction with summaries of our previous results obtained on the kinetic pathway of shish-kebab formation under the shear flow (parts B, C, and D).[21] We aim to explore structure evolution along the spinning line of fibers spun from the homogeneous, entangled UHMWPE/decalin solutions to clarify the kinetic pathways leading to the shish-kebab structure (Figure 1A). In the spinning process, a homogeneous solution extruded from a spinneret is subjected to a complex flow field with increasing total strain or work done by the flow and with decreasing temperature along the spinning line. Our objectives in this work are to clarify the following two problems: How do the flow-induced structures evolve along the spinning line (Figure 1A)? Are the flow-induced structures appeared along the spinning line similar to or different

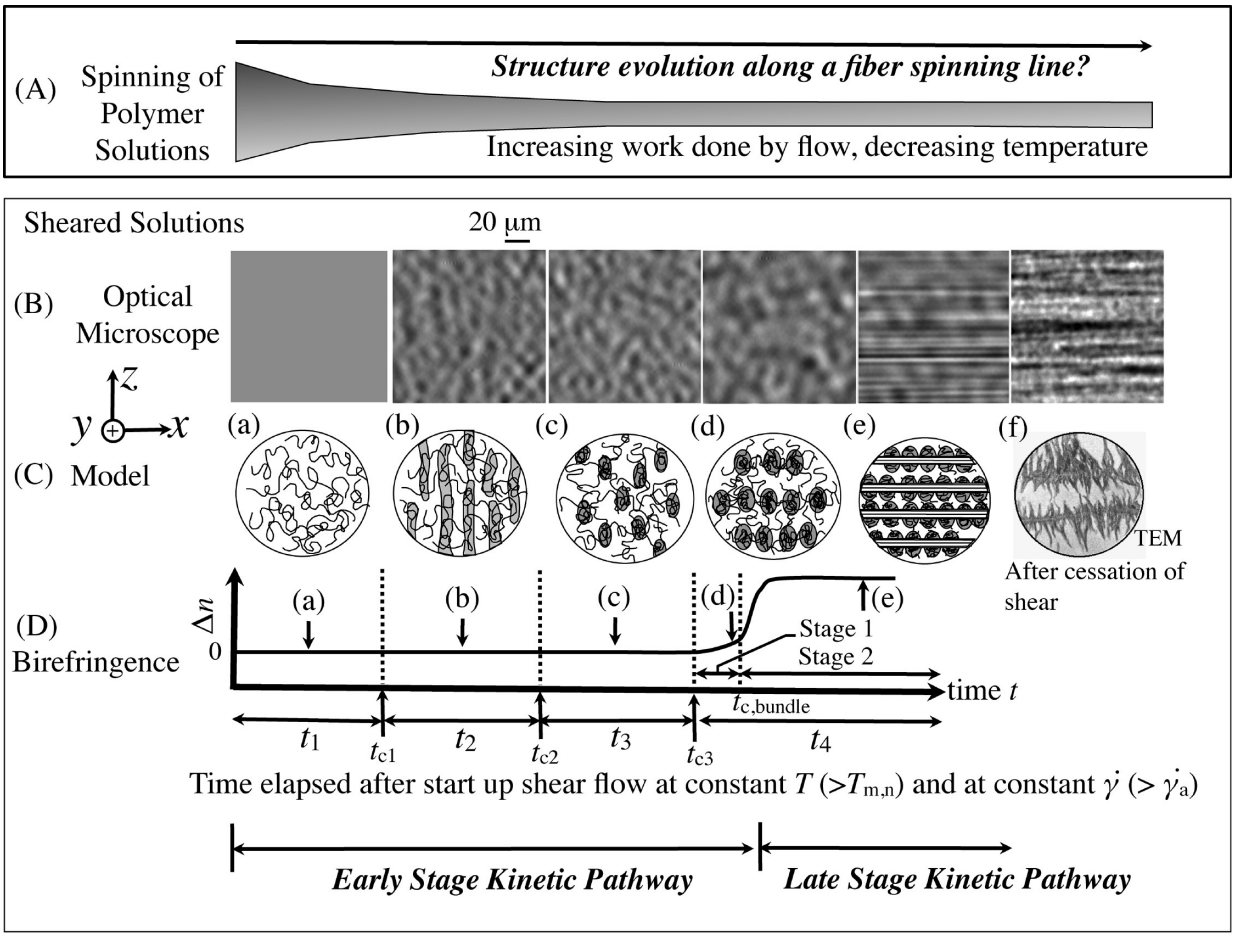

Figure 1. Schematic illustration of objectives of this work on off-line TEM observations of structures evolved along spinning lines of fibers spun from the homogeneous, entangled UHMWPE solutions (part A) and summaries of the previous results,[20,21] obtained from the online observations of the time evolution of the structures in UHMWPE solutions after imposing step-up shear flow (B to D), which motivated the present work. This work particularly focuses on the structure evolutions occurring in the early stage kinetic pathway which exists at $t < t_{c,bundle}$ before the onset of the crystallization into the shish-kebab structure (in the late stage kinetic pathway).

from the time-evolution of the shear-induced structures observed after a step up shear from $\dot{\gamma} = 0$ to $\dot{\gamma} > \tau_e^{-1}$ at a constant temperature T higher than the nominal melting temperature $T_{m,n}$ of the solutions as summarized in parts a to e in parts B−D of Figure 1? Parts B and C of Figure 1 show the online transmission optical micrographs (OM) and their sketches, respectively, where the *x*-, *y*-, and *z*-axes are taken parallel to the flow, velocity gradient, and neutral (or vorticity) directions, respectively, while Figure 1D shows the time evolution of Δn.

The entire time-evolution process of self-assembling structures after imposing the step-up shear flow on the homogeneous solutions is classified into four time regions t_1 to t_4 as detailed previously[21] and in parts B−D of Figure 1. In region t_1, where time $t < t_{c1}$, t_{c1} being the characteristic time for the solvent squeezing,[21] the entangled polymer networks swollen with solvent are uniformly deformed, and hence the sheared solution remains essentially homogeneous, so that OM image is featureless, showing no remarkable structures as shown in Figure 1B(a). In region t_2 where $t_{c1} \leq t < t_{c2}$, t_{c2} being the characteristic time for formation of the demixed domains,[21] we discerned the OM image in Figure 1B(b) which essentially represents the plane-wave type concentration fluctuations with their wave vectors oriented along the flow direction as indicated by the sketch in Figure 1C(b), where the shaded and unshaded regions represent those rich and poor in polymers, respectively. In region t_3 where $t_{c2} \leq t < t_{c3}$, t_{c3} being the characteristic time for the string formation,[21] the image in Figure 1B(c) is discerned, which suggests formation of the demixed domains whose centers of mass are randomly distributed in space, as sketched in Figure 1C-(c). In region t_4, where $t \geq t_{c3}$, the demixed domains are aligned into the string-like assemblies oriented parallel to the flow direction, as shown in the Figure 1B(d) and the sketch in Figure1C(d). In the string phase, the strings are aligned side by side laterally (along the direction perpendicular to the flow direction), so that the centers of mass of the demixed domains are nematically aligned parallel to the flow direction.

It should be stressed that the Δn is very small up to time region t_3 compared with that in stage 2 in time region t_4 and is still small in stage 1 in time region 4 as schematically shown in Figure 1D, so that polymer chains themselves are essentially in random coils up to this stage (stage 1 in time region t_4) even under the flow. The observed drastic increase in Δn (between the end of stage 1 and the steady state in stage 2) by a factor of about five times[21] in region t_4 across $t_{c,bundle}$, the characteristic time for formation of the bundles of the stretched chains, leads us to further classify this region into two stages: stage 1, where Δn becomes slightly more

dx.doi.org/10.1021/ma2008817 |*Macromolecules* 2011, 44, 7335–7350

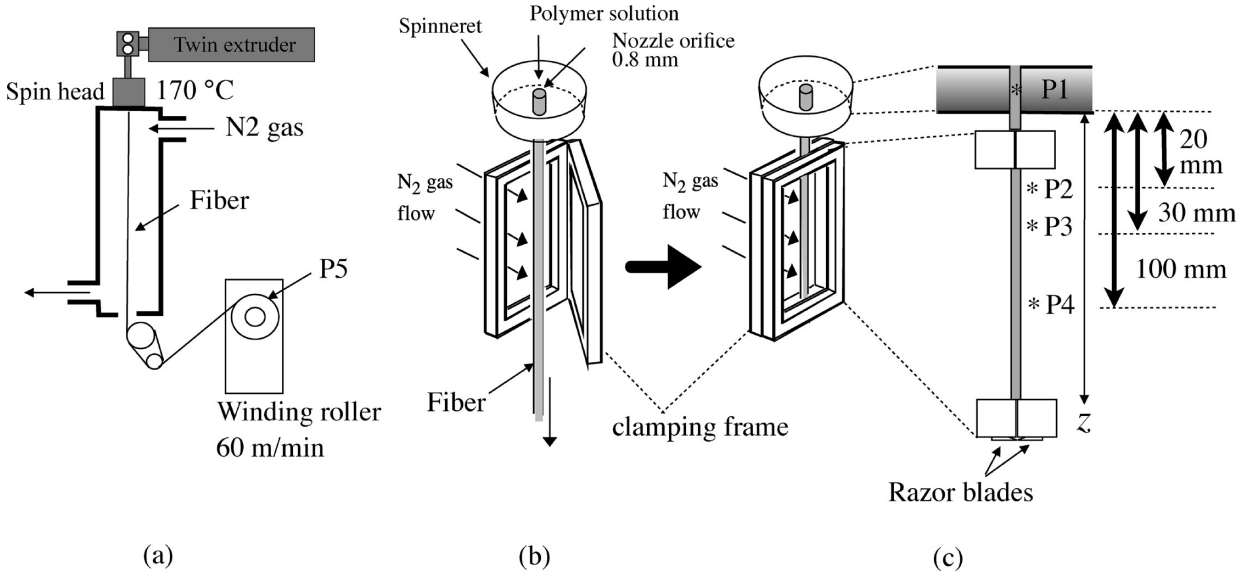

Figure 2. (a) Schematic illustration of the fiber spinning process of the homogeneous UHMWPE/decalin solutions prepared with a twin extruder. The extruded solution at 170 °C with the throughput rate =1 g/min was drawn into a fiber with the take-up velocity of 60 m/min; The fiber running through the spinning line was cooled down with the nitrogen gas at room temperature. (b) A part of the fiber running through the spinning line was quickly sampled out from the spinning line with a pair of frames having razor blades at its upper and lower edges; The specimen fixed by the frame was quickly cooled to room temperature with a nitrogen gas flow for the solidification. (c) The structures evolved in the solidified specimens at positions P1 to P4 shown in part c as well as at position P5 in part a were investigated under TEM after the fixation process illustrated in Figure3.

positive than that in the time regions t_1 to t_3, so that the strings have only a weak Δn, and stage 2, where Δn sharply increases with time. This Δn uprise reveals that the bundles of the stretched chains interconnecting the demixed domains start to be formed parallel to the string as illustrated by the straight lines as shown in sketch (e) in Figure 1C, thereby the string starts to have a strong optical anisotropy. Image f in Figure 1B represents the OM image taken in-situ at 124 °C after cessation of the shear flow, and the structure is proved to be the shish-kebab structure by the ex-situ TEM observation on the specimen cooled to room temperature, as shown in Figure 1C(f)[21].

The building up of the plane wave concentration fluctuations mediated by the stress-diffusion coupling is well established by the HFMO theory.[24−26] When the plane wave concentration fluctuations, which are convected around the z-axis, are investigated with the small-angle light scattering (SALS) with the incident laser beam along the y-axis, the SALS pattern in the q_x and q_z plane shows the butterfly pattern with their wings oriented along the x-axis and spreading only a little along the z-axis.[19,43,44] Here q_x and q_z are the x- and z-component of the scattering vector **q**. This particular shape (see Figure 12b in ref 43) of the butterfly type SALS pattern is consistent with the plane-wave concentration fluctuations on the $x-z$ plane as illustrated in Figure 1C(b).

In this paper we shall present a full account of structure formation along the fiber spinning line to elucidate the kinetic pathway and mechanism of shish-kebab formation, including the CSCT triggered at a special, localized place within the phase-separated structure. We especially aim to clarify the early stage kinetic pathway and the detailed structures evolved therein.

3. EXPERIMENTS

3.1. Materials. The polymer used is an ultrahigh molecular weight linear polyethylene (UHMWPE, Hizex 240M, Mitsui Chemicals, Tokyo, Japan) having weight-average molecular weight $M_w = 2.0 \times 10^6$ and heterogeneity index $M_w/M_n = 12$, where M_n is number-average molecular weight. The typical polymer solutions studied had concentration c = 10.0 wt % ($c/c^* = 20$) in decalin as a solvent, where c^* is the overlap concentration. The concentrated UHMWPE solutions were prepared by mixing UHMWPE, decalin, and an antioxidant agent (2,6-ditert-butyl-p-cresol) by an amount of 1 wt % of the total solution, at 210 °C by using a twin screw extruder. Small impurities insoluble to the solutions were filtered off by a mesh filter (400 lines/inch).

3.2. Fiber Spinning. The off-line observations of the superstructures developed in the UHMWPE/decaline solution along the fiber spinning lines were conducted with transmission electron microscopy (TEM). The fiber spinning process involves an extrusion of the homogeneous decalin solutions prepared by a twin-screw extruder through a spinneret, having an orifice diameter of 0.8 mm, controlled at 170 °C, with the throughput rate of 1 g/min. The extrudates were drawn into fibers with a take-up velocity of 60 m/min, while they were cooled down by the nitrogen gas at room temperature as shown in Figure 2a.

3.3. Sampling of Fiber Specimens from the Spinning Line. In order to explore the flow-induced structures developed along the fiber spinning line, a part of the fiber running through the spinning line was quickly sampled out from the spinning line with a pair of frames having razor blades at its upper and lower edges to cut off and clamp the running fibers (Figure 2b). The specimen fixed by the clamping frame was quickly cooled to room temperature with a nitrogen gas flow for solidification. This "solidification" process itself involves crystallization in the structures developed in situ in the fiber in the spinning line. We sampled the specimens from the solidified fiber at four positions P2 to P5 defined in Figure 2, parts a and c. Positions P2, P3, and P4 were located at z = 20, 30, and 100 mm, where z is defined as a distance along the spinning line with an origin at the surface of the spinneret (z = 0). P1 represents the sampling of the solution before the extrusion. However the sample P1 was actually obtained as follows: The solution was extruded from the orifice at the same temperature (170 °C) and with the same rate of throughput (1 g/min) and the freely fallen solution under the gravitational force was received on a flat plate set at 50 mm

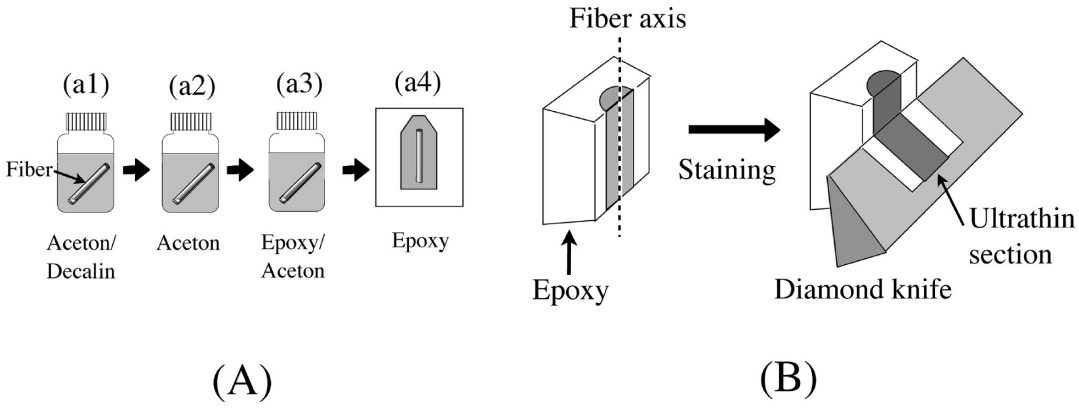

Figure 3. (A) Fixation process of the solidified specimens swollen with the solvent involves first the stepwise solvent replacement from decalin to acetone (parts a1 to a2), then acetone to epoxy monomer (part a3), and finally the epoxy monomer into epoxy resin at 60 °C for ∼8 h (part a4). (B) A block of the epoxy resin was trimmed to expose the inner region of the fiber for staining with RuO_4 vapor for 10 h at room temperature. The stained specimen was cut into ultrathin sections of thickness of approximately 70 nm parallel to the fiber axis with a diamond knife. The ultrathin sections had the size of ∼2 mm along the fiber axis and contained a whole fiber in the direction perpendicular to the fiber axis.

below the orifice. The solution was cooled down to room temperature and crystallized on the plate without an excess deformation. The samples obtained from positions P1−P4 were expected to retain, at the large length scale of our observation, the original structures evolved in the spinning line through the solidification process via crystallization: The structures observed in the solidified specimens, especially those at the length scale greater than the lamellar crystals evolved in the solidification process are anticipated to reflect online (in situ) structures evolved along the spinning line. This is simply because the large-length scale structures relax slower than the solidification rate (the diffusion-limited solidification criterion). The structure developed at the end of the spinning line was sampled at position P5 at a winding roller (Figure 2a).

3.4. Fixation of Internal Structures of Fiber Specimens Swollen with Solvent. The solidified specimens taken out from the spinning line at the positions P1 to P4 are gel-like and swollen with the solvent with its amount close to but less than 90 wt %, while the specimen taken out at the position P5 contains about 30 to 50 wt % of the solvent. The solvent must be completely removed before TEM observations without changing the structures developed in the as-sampled spun fibers. For this purpose the solvent was first exchanged to acetone at room temperature by repeating a stepwise soaking of the specimen into an acetone/decalin mixture, in which the composition of acetone/decalin was stepwisely changed from 10/90 to 100/0 wt/wt (as shown in part a1 and part a2 in Figure 3A). Acetone was then exchanged to epoxy monomer by using the same solvent exchange procedure as described above (as shown in part a3 and part a4 in Figure 3A). The epoxy monomer was then cured into epoxy resin at 60 °C for ∼8 h (part a4 in Figure 3A). We define this process including both the solvent exchange and the curing as the "fixation process". This process should be distinguished from the process defined as the "solidification" in section 3.3. The fixation process were confirmed to hardly affect the structures developed in the solidified fibers as will be shown later in section 4.1.

3.5. TEM Observations. A block of the epoxy resin, in which the solidified fiber specimen was embedded, was trimmed to expose the inner region of the fiber for staining with RuO_4 vapor for 10 h at room temperature. The stained specimen with the length along the fiber axis of ∼2 mm which includes the whole fiber along its width direction was cut into ultrathin sections of approximately 70 nm in thickness parallel to the fiber axis with a diamond knife mounted on an ultramicrotome (Ultratome V, LKB Co., Ltd.) at room temperature (Figure 3B). The sliced sections were prepared in such a way that they contain the central part of the fiber in the middle of them and mounted on carbon-coated poly(vinyl formal) film on copper grids for TEM observations with JEM-200CX (JEOL, Tokyo, Japan) operated at 100 kV.

4. RESULTS: STRUCTURE EVOLUTIONS ALONG THE SPINNING LINE: OFF-LINE TEM OBSERVATIONS ON THE SPECIMENS SUBJECTED TO THE SOLIDIFICATION AND FIXATION

4.1. Conservation of the Solidified Structures before and after the Fixation. We conducted small-angle light scattering (SALS) and OM experiments in order to compare the structures in the solidified samples before and after the fixation to confirm the conservation of the structures during the process (Figure 4). For this purpose, we did not use the fiber, because a round shape of the fiber is not suitable for SALS. Instead, the same UHMWPE solution was subjected to a given shear flow with a parallel plate fixture at a gap distance of 30 μm by using the shear apparatus described elsewhere.[45] The solution was first kept at 160 °C for 10 min and subsequently cooled down to 118 °C ($>T_{m,n}$ =115−119 °C) at which a shear flow was imposed for 240 s. After the cessation of the shear, the solution was cooled down to room temperature for the solidification of the shear-induced structures: the gel-like sample thus obtained was first carefully removed from the shear cell without an excess deformation and then soaked in decalin to prevent drying. A small piece of specimen (∼25 mm^2) was cut out from the sample at the specified position (subjected to $\dot{\gamma}$ = 9.3 s^{-1}) from the center of the sample with a sharp blade. The specimen was embedded in epoxy resin after the same "fixation" process as described earlier.

In Figure 4, the upper and lower rows demonstrate the SALS patterns and OM images taken for the solidified specimens before (a1 and b1) and after the fixation process (a2 and b2), respectively. The arrow shown in the left bottom corner of the SALS pattern in part a1 represents the flow direction commonly for all the SALS patterns and OM images. The scales inserted in the SALS pattern and OM images in part a1 are also common for all the SALS patterns and OM images, respectively. The optical axes of both the polarizer and the analyzer set in front of and after the specimens, respectively, denoted by the arrows labeled with "P" and "A", respectively, were set perpendicular to the flow direction in parts a1 and a2 (defined as H_H polarization), while

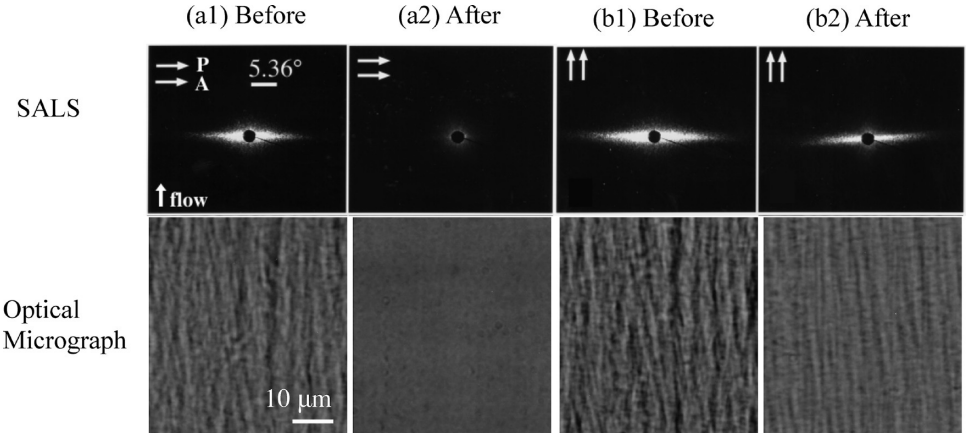

Figure 4. Upper and lower rows demonstrate the SALS patterns and OM images taken for the solidified specimens before (a1 and b1) and after the fixation process (a2 and b2), respectively. The arrow shown in the left bottom corner of the SALS pattern in part (a1) commonly represents the flow direction for all the SALS patterns and OM images. The scales inserted in the SALS pattern and OM images in part (a1) are also common to all the SALS patterns and OM images, respectively. The optical axes of both the polarizer and the analyzer are denoted by the arrows labeled with "P" and "A", respectively.

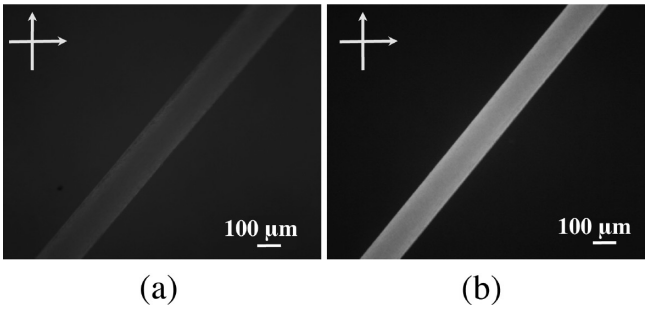

Figure 5. Typical appearance of the solidified and fixed fibers at positions P2−P4−1 (part a) and P4−2−P5 (part b) under the crossed polarizers shown by the arrows.

they are set parallel to the flow direction in part b1 and b2 (defined as V_V polarization).

Under H_H polarization, the refractive index of the polymer $n_{p\perp}$ (1.545) is larger than the solvent n_s (1.4758) before the fixation,[46,47] so that we can observe the fibrillar structure in the OM image and the corresponding streak-like scattering pattern oriented parallel and perpendicular to the flow direction, respectively (Figure 4a1). However, after the fixation the refractive index of the matrix phase of the fibrillar structure increased from n_s to n_{ep} (the refractive index of the epoxy resin, 1.55−1.60) ∼ $n_{p\perp}$,[46,47] so that both the SALS pattern and the OM image disappear (Figure 4a2). On the other hand under V_V polarization, the refractive index of the fibrillar structure satisfies $n_{p\parallel} > n_s$ before the fixation, and $n_{p\parallel} > n_{p\perp} \sim n_{ep}$ ($>n_s$) after the fixation, so that we can discern the streak-like SALS patterns and the fibrillar structures in the OM images both before and after the fixation, as shown in Figures 4b1 and 4b2, respectively. It is important to note that the same patterns and images were observed before and after the fixation, except for the natural difference in the intensity and contrast, respectively. These results ensure the no changes in the solidified structures throughout the fixation processes.

4.2. Birefringence Variation along the Spinning Line. Birefringence of the extruded solution from the nozzle must be nearly zero at the position P1, and it would increase along the spinning line due to the structure evolutions in the fiber spinning process.[48,49] In this work, we conducted the off-line measurement of birefringence $\Delta n(z)$ for the solidified fiber as a function of the distance z from the spinneret. We believe that the $\Delta n(z)$ found for the solidified fiber qualitatively reflects a relative change in Δn with z for the fiber in the spinning process. Figure 5 shows the optical appearance of the fiber after the solidification and the fixiation under the crossed polarizers with their polarization axes as indicated by the arrows. Parts a and b in Figure 5 represent the typical optical appearance of the fiber sampled at the position from P1 to P4−1 ($z \leq 100$ mm) and from P4−2 to P5 ($z > 100$ mm), respectively (see the definition of P4−1 and P4−2 later in conjunction with Figure 13). The brightness of the fiber in part b is found to be much higher than that of part a. It is worthy of noticing that Δn may increase due to post crystallization induced by the solidification process. The small Δn observed in part a thereby suggests that the Δn observed in situ along the spinning line at positions from P1 to P4−1 must be even smaller than that expected from part a. Contrary to part a, the higher brightness observed in part b clearly suggests a lager $\Delta n(z)$ developed in situ in the spinning line from P4−2 to P5. Thus, we qualitatively conclude the online $\Delta n(z) \sim 0$ at $z < 100$ mm and $\Delta n(z) > 0$ at $z \geq 100$ mm. The uprise in Δn in stage 2 (to be discussed later in conjunction with Figure 13) is large, at least about a factor of 3.

4.3. Structures in the Quiescent Solutions. Parts a1 and a2 of Figure 6 show the TEMs of the solution solidified and fixed at P1 taken by using the method detailed earlier in section 3.3. Darker regions in the micrograph are the region rich in polyethylene stained with RuO_4 and bright region is the region rich in epoxy resin which was originally filled with decalin. Many dark fibrous structures are spread into whole area in the micrograph in part a1. However the regions labeled by A, B, and C are rich in the dark fibrils. This heterogeneous dispersion of the dark fibrils may suggest frozen thermal concentration fluctuations inherent in the solution before the solidification process or those enhanced by the solidification process. Figure 6a2 is an enlarged view of the fibril-rich region in part a1, showing stacks of lamellae with their normals (vectors normal to the chain-folding surface of the lamellae) parallel to the surface of the ultrathin section (edge-on lamellae in region D) and perpendicular to the surface (region E).

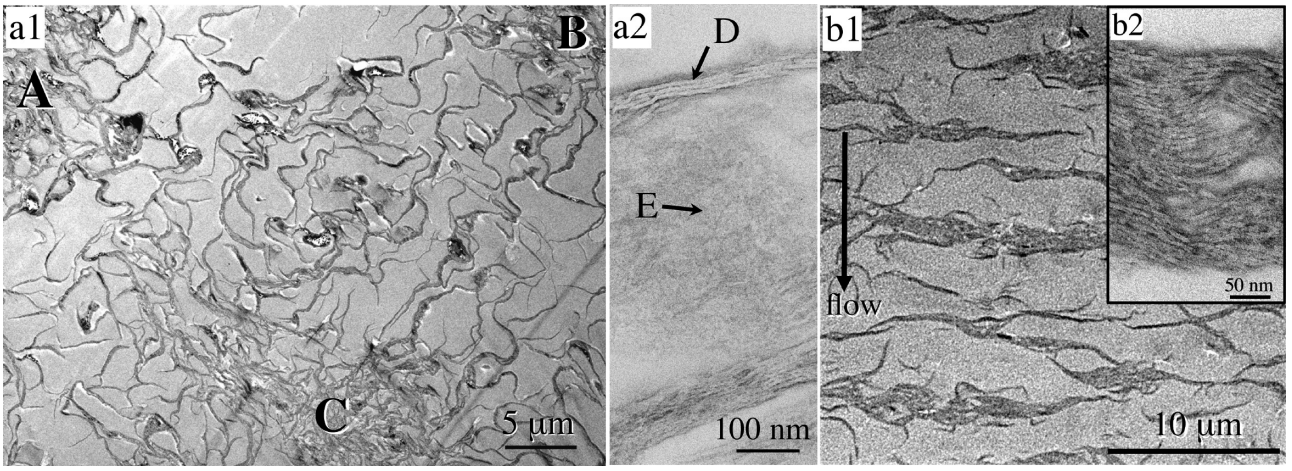

Figure 6. Low-magnification TEM image of the specimen at position P1 (part a1) and a zoom-in image of part a1 (part a2). The specimen was stained by RuO_4 and darker regions are rich in polyethylene and bright regions are rich in epoxy resin which corresponds to decalin before the fixation. The regions marked with A,B, and C in part a1 reflect the regions rich in UHMWPE. Normals of lamellar crystals are oriented parallel and perpendicular to the surface of the ultrathin section in the region "D" and "E" of part a2, respectively. A low-magnification TEM image of the plane-wave concentration fluctuations observed at position P2 located at 20 mm down stream from the spinneret (part b1), and a zoom-in image of the polymer-rich region in part b1 (part b2).

Table 1. Variations of Average Lamellar Thickness and Spacing along the Spinning Line

	P1 solidified quiescent solution	P2 plane wave	P3 demixed domain	P4 string (stage 1)	P5 shish-kebab
lamellar thickness D (nm)	5.9 ± 0.9	5.9 ± 1.0	5.6 ± 0.7	5.3 ± 1.0	7.5 ± 0.9
lamellar spacing L (nm)	7.9 ± 0.9	8.8 ± 1.6	8.8 ± 0.6	8.1 ± 1.1	10.1 ± 0.9

The polymer chains in the solution must segregate into lamellar crystals during the solidification process and appeared dark fibrous structures as shown in part a1. We expect that the spatial distribution of the lamellae at the length scale larger than lamellae themselves, as shown in part a1, reflects essentially the large-length-scale concentration fluctuations of polymer chains before the solidification process of the solution within the criterion of the diffusion-limited solidification. The average lamellar thickness D and lamellar spacing L is 5.9 and 7.9 nm, respectively (see column P1 in Table 1). We calculated also the standard deviation for the lamellar thickness and long period. The standard deviation of the lamellar thickness is 15−20% with respect to its average. Within the experimental accuracy, the thickness of lamellae and its standard deviation are almost independent of the positions P1 to P4 along the spinning line. The lamellae thickening occurs at position P5, which will be discussed later in section 5.4 in conjunction with Figure 15.

4.4. Plane-Wave Type Concentration Fluctuations (Position P2). Figure 6b1 shows a typical TEM taken at P2 located at z = 20 mm down stream from the nozzle. It is expected to reflect the plane-wave type concentration fluctuations induced by the flow with their wave vectors parallel to the flow direction which are frozen by the diffusion-limited solidification due to crystallization. Polymer-rich regions appear dark and solvent-rich regions appear bright in the micrograph. The dark region is composed of the stacks of lamellae of $D \sim 5.9$ nm and $L \sim 8.8$ nm (Table 1), as clearly elucidated in the inset to Figure 6b2. It is worth noting that the normals of the lamellae are mostly aligned parallel to the wave vector and hence the flow direction. We believe that the preferential orientation of the lamellae must be a consequence of the crystallization induced by the concentration gradient of UHMWPE in the plane-wave type concentrations fluctuations along the flow direction but not due to chain-orientation-induced crystallization. This will be discussed again in section 5.5. Interestingly the off-line TEM image shown in part b1 is essentially consistent with the online OM image shown in Figure 1B(b).

4.5. Demixed Domains (Position P3). Figure 7(a) shows a typical TEM observed for the specimen at P3 located at z = 30 mm down stream from the nozzle. In the image, the polymer-rich domains appear dark due to a selective staining with RuO_4, while the solvent-rich matrix phase appears bright. The TEM image reveals that the polymer-rich domains are extended perpendicular to the flow direction, suggesting an oblate-ellipsoidal shape with the axis of revolution oriented parallel to the flow direction and their mass centers are randomly aligned in space. Interestingly the off-line TEM image is similar to the online OM image shown in Figure 1B(c). Figure 7b zooms in the polymer-rich domain itself. It elucidates that the lamellar crystallization served for the solidification of the demixed domains existed in situ at P3. Part c in Figure 7 shows the zoom-in image of the boundary region of the demixed domain which is encompassed by the small solid black rectangle in part b. The demixed domains are shown to be composed of lamellar stacks with $D \sim 5.6$ nm and $L \sim 8.8$ nm (Table 1). The normals of lamellae are preferentially aligned perpendicular to the interface of the demixed domain and the matrix. This preferential orientation of lamellae suggests again the lamellar crystallization controlled by the boundary interface as in the case of the lamellar crystallization in the plane-wave type concentration fluctuations, as will be discussed in detail in section 5.5 later.

dx.doi.org/10.1021/ma2008817 |*Macromolecules* 2011, 44, 7335–7350

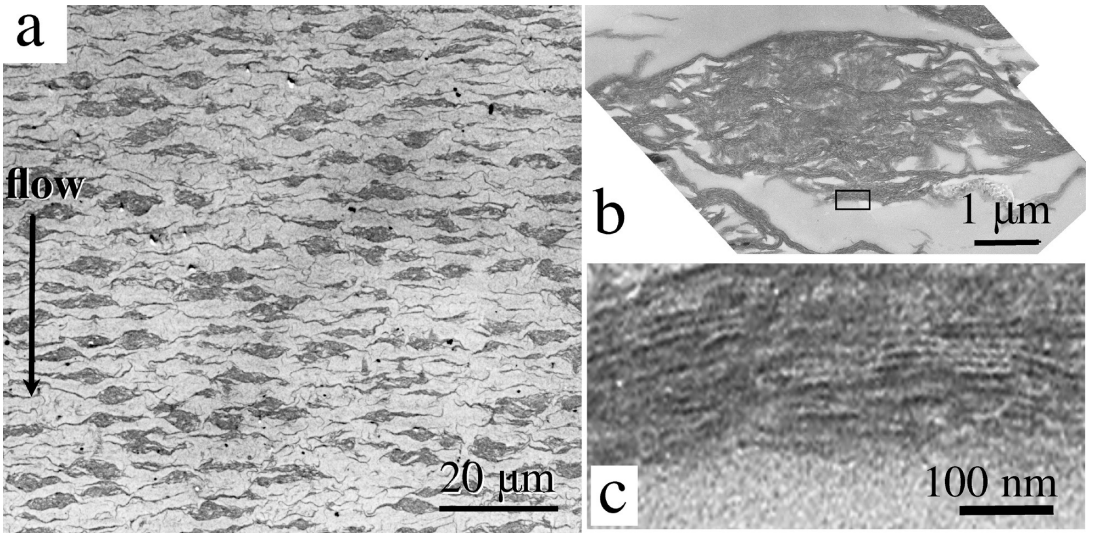

Figure 7. TEM images of the fiber at P3 located at 30 mm down stream from the spinneret: (a) a low magnification image, (b) a zoom-in image of a demixed domain, and (c) a zoom-in image of a part of the demixed domain encompassed with a black rectangle in part b.

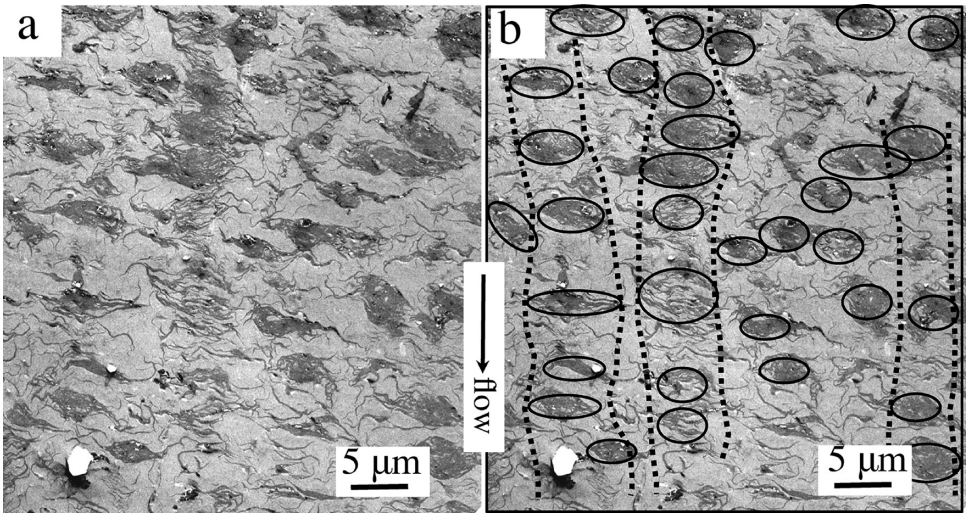

Figure 8. TEM images of the fiber at P4 located at 100 mm down stream from the spinneret: (a) onset of the string formation and (b) the same image as part a, where the string-like assemblies and demixed domains in the strings are sketched by broken lines and black ellipses, respectively.

4.6. String-Like Self-Assembly of Demixed Domains (Position P4). At P4 located at $z \sim 100$ mm from the nozzle, the demixed domains start to align with their centers of mass in rows parallel to the flow-direction, as typically shown in Figure 8a. Part b is the same micrograph as part a, but it highlights the string-like self-assemblies and the demixed domains inside the strings with the broken black lines and the solid black ellipses, respectively. Interestingly, the off-line TEM image is similar to the online OM image shown in Figure 1B(d). About three string-like assemblies of the demixed domains appear in Figure 8a as sketched in Figure 8b, but there are still some domains which are off-aligned from the strings. The trend for formation of the well-defined assembly of demixed domains into strings was found in a down-stream portion of the ultrathin-section obtained at P4, as will be shown in the next section (Figure 9). The averaged lamellar thickness and long period are 5.3 and 8.1 nm, respectively, as summarized in Table 1.

4.7. Densification of Demixed Domains in the Strings and Densification of the Strings Themselves in the Fiber. TEM images shown in Figure 9 were obtained slightly at a down-stream side in the ultrathin section in comparison with that shown in Figure 8. The following two tendencies are worth noting in Figure 9 with respect to the process and mechanism of string-like structure formation: (1) a densification of the demixed domains within the strings and (2) a densification of strings themselves within the fibers. Part c in Figure 9 is a micrograph which clearly captures evidence for the former densification process (1). The domains marked by A, B, and C are going to be incorporated into the string, driven by the hydrodynamic interactions which will be discussed later in section 5.3 in detail. As a consequence of the hydrodynamic effects, strings S1 to S4 shown in part a have a higher density of the demixed domains than those shown in Figure 8b. Furthermore, the strings themselves tend to be densified; the clusters of the strings in the area

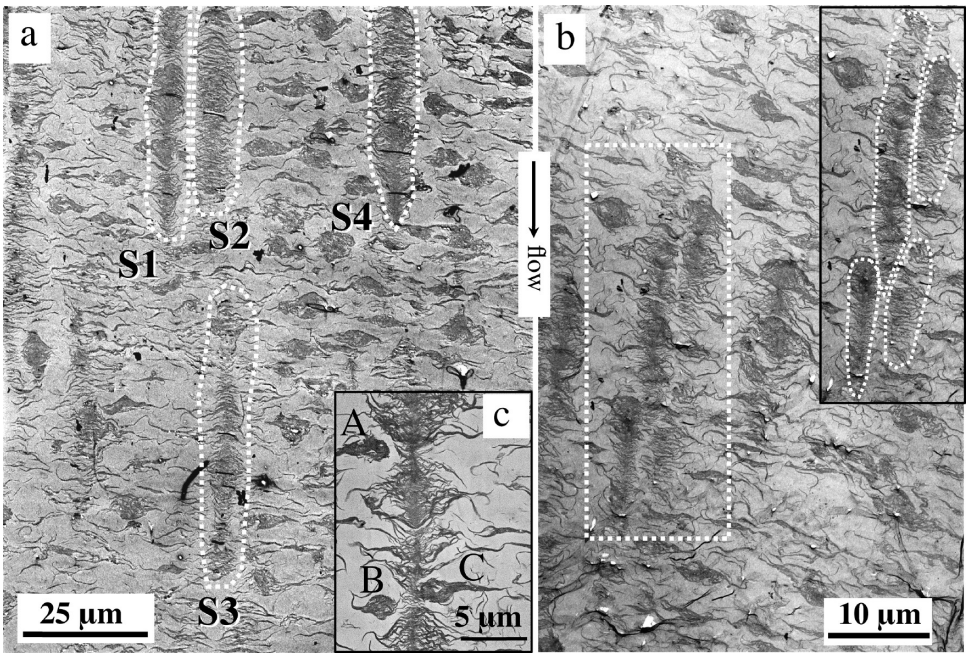

Figure 9. Densification of the demixed domains in the string-like structure (a) and densification of the string-like structures themselves within the fiber (b): (a) Four strings denoted by S1 to S4 in part a are composed of the densified demixed domains. (b) The clusters of the strings encompassed by the white broken rectangle in part b are composed of four strings as sketched by the white broken lines in the inset of part b. (c) Off-aligned domains marked by A, B, and C tend to be incorporated into a string driven by the hydrodynamic interactions, resulting in densification of the strings.

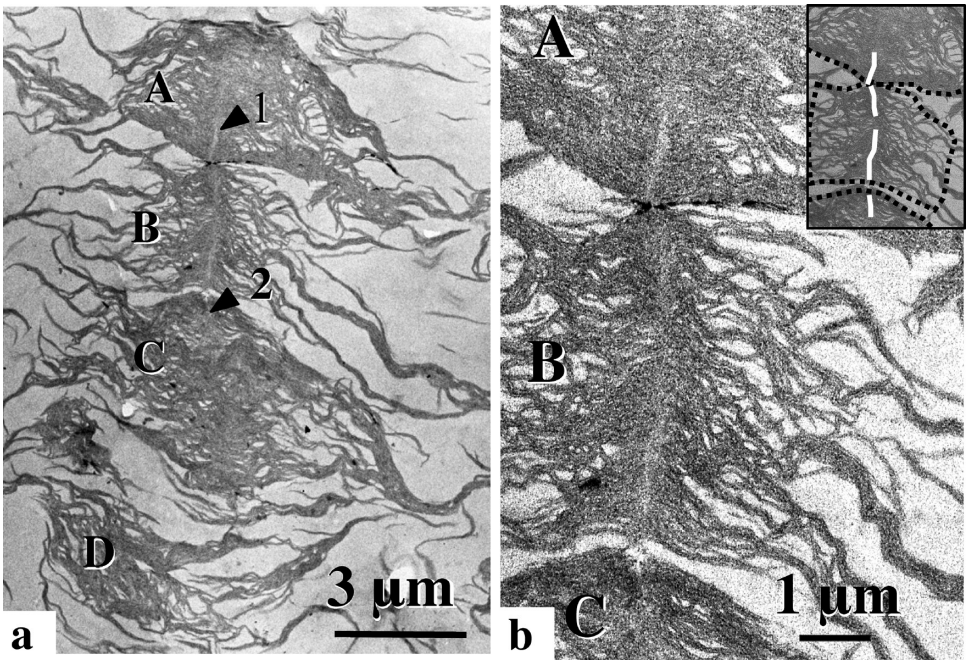

Figure 10. TEM micrograph of the solidified specimen sampled at P4 and an assembly of demixed domains, suggesting shish-formation from the boundaries of the impinged demixed domains. Part a elucidates the string-like assembly of the demixed domains A to D which suggests formation of shishs, extending between the two arrows labeled 1 and 2, which are grown from the boundary of the impinged domains A and B and from that of B and C. Part b is the zoom-in image of part a. The inset in part b encompassed by a black rectangle at the upper right corner defines the three domains (broken black lines) and two shishs (white solid lines).

encompassed by the white broken line in Figure 9b are composed of four strings which are both laterally and longitudinally self-assembled closely one another, as sketched in the inset to Figure 9b, where the four strings are encompassed by the white broken lines. This densification process of strings will be also discussed later in section 5.3.

4.8. Coil-to-Stretched Chain Transition and Nucleation of Shishs. Figure 10 shows a TEM micrograph obtained from the

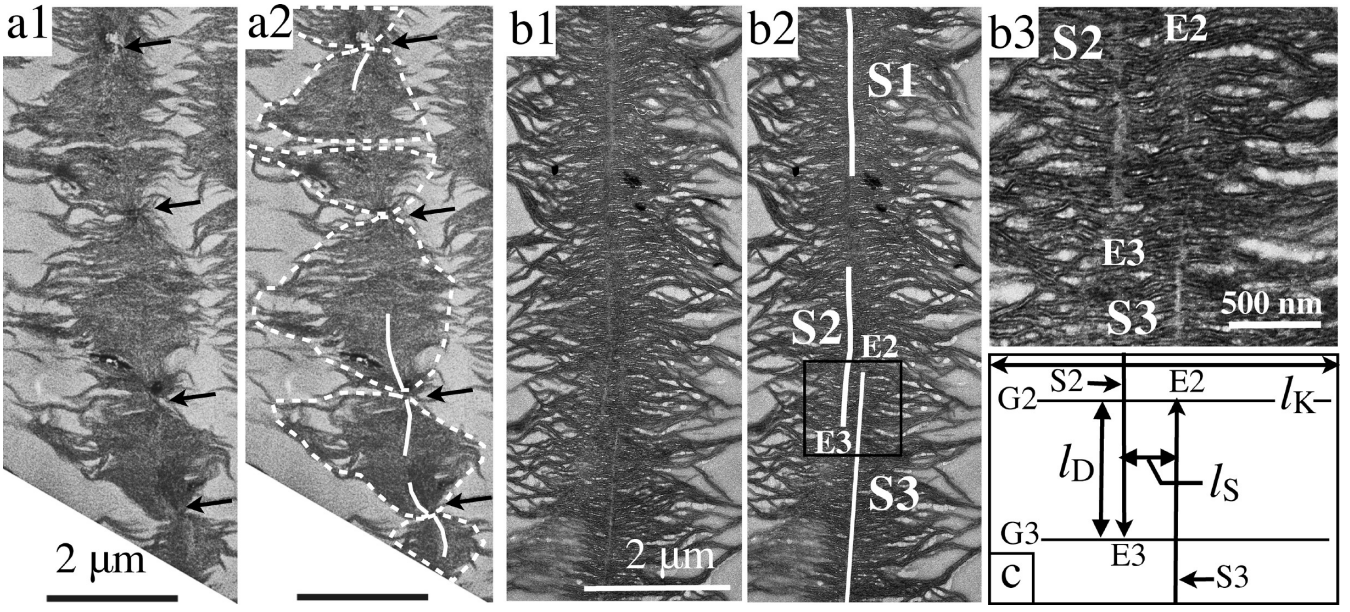

Figure 11. Example of the string-like assembly of demixed domains suggesting the shish formation from the boundary of the impinged demixed domains (part a1) and its sketch (part a2). Black arrows in parts a1 and a2 indicate the bridging domains at the boundaries of the impinged demixed domains, while broken white lines and solid white lines in part a2 sketch boundaries of domains and shishs, respectively. Part b1 and its sketch (part b2) elucidate a growth of shishs (as sketched by S1 to S3) along the fiber axis together with the decay of the memory of the demixed domains. Part b3 shows a zoom-in image of the part of the region in part b2, which is encompassed by the black rectangle, while part c sketches the image shown in part b3: the growth fronts of the shishs S2 and S3 stop at E3 and E2, respectively, by interferences of the growing fronts of kebab lamellae G3 and G2 overgrown from S3 and S2, respectively. In the space between the two planes G2 and G3 with a distance l_D apart, the kebab lamellae are expected to overgrown from a double strands of shishs. We judge the shish S3 is continuous from the bottom up to E2 in image b3.

specimen sampled at position P4 but a slightly more down-steam side than the position where Figure 9 was taken. Part a elucidates the string-like assembly of demixed domains A to D which suggests formation of shishs, extending between the two arrows labeled 1 and 2, which are seemingly grown from the boundary of the impinged domains A and B and from that of B and C. Part b shows a zoom-in image of the domains A to C in part a, which visualizes two shishs connecting the three domains. The inset encompassed by a black rectangle in the top right corner of part b sketches the three domains highlighted with broken dark lines and two shishs highlighted with white solid lines. Shishs are found to grow from the boundaries of the impinged demixed domains toward their interiors, though the two shishs in domain B does not yet seem to be interconnected within the B domain, as sketched by the two white lines in the inset. The interconnected domains with shishs are thought to be the precursory structure of shish-kebab, because they contain the shishs and the kebab lamellae overgrown from the shishs. It is of worthy noting that the precursory structure still retains the memory of the demixed domains.

Figure 11a1 and its sketch (part a2) also indicate an example of the string-like assembly of demixed domains which suggests the shish formation from the boundaries between the two impinged domains. Black arrows in parts a1 and a2 indicate the boundaries, while the broken white lines and solid white lines in sketch a2 indicate boundaries of domains and shishs, respectively. One can visualize that : the domains are so densified in the string that the neighboring domains are interconnected at their boundaries with narrow bridging domains; three shishs grow from respective boundaries between the impinged domains toward their interiors. Figure 11b1 taken at $z > 100$ mm, a more down-stream side of P4, and its sketch (part b2) elucidate a growth of shishs (as sketched by S1 to S3) along the fiber axis together with the decay of the memory of the demixed domains and their boundaries within the string-like structure, due to progress of the densification of demixed domains and the long-range rearrangements of polymer chains within the string.

It is worth noting that several numbers of shishs are observed in a single string-like structure. In part b1, three shishs, as sketched by white lines labeled with S1 to S3 in part b2, are found in the single string-like structure. The three shishs must be a consequence of the multiple nucleations of shishs from the bundles of stretched chains formed at the boundaries of the impinged demixed domains in the string-like structure as shown in parts a1 and a2 in Figure 11. It may be feasible that the shishs S1 and S2 are interconnected in the space on the top surface or below the bottom surface of the ultrathin section. Figure 11b3 shows the zoom-in image of the area encompassed by the black rectangle in Figure 11b2. Two shishs (S2 and S3) seem to grow from the opposite directions (from the top and the bottom of the image), to pass by each other, and to stop growing at the points E3 and E2, respectively. To understand this interrupted growth of the shishs, we have to consider a timing of growth of both shishs and kebabs. Kebabs must be overgrown from shishs, and the growth front of the kebabs must follow the growth front of the shishs with some distance behind. Therefore, in the case of multiple nucleations of shishs in a single string-like structure, the growth of the shishs S2 and S3, separated by a lateral distance l_S much smaller than the lateral width l_K of kebabs, must be stopped at points E3 and E2, respectively, where the growth fronts of S2 and S3 interfere with the growth front of the kebab lamellae G3 and G2 overgrown from S3 and S2, respectively, as schematically shown in part c. In the intervening space with a distance l_D apart

dx.doi.org/10.1021/ma2008817 |*Macromolecules* 2011, 44, 7335–7350

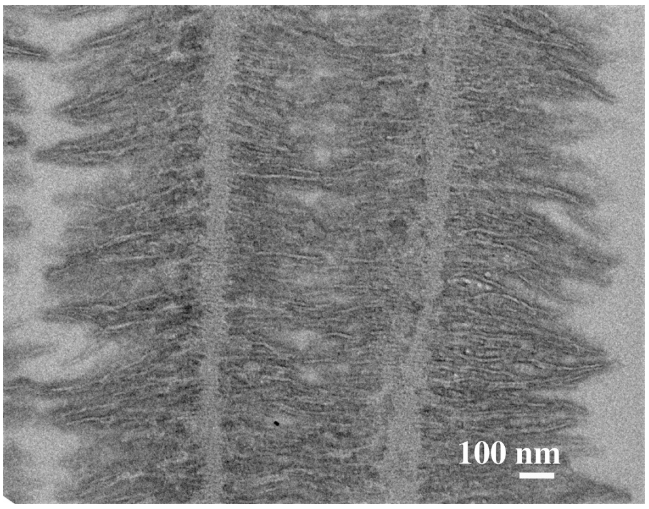

Figure 12. Typical TEM image of shish-kebabs observed in the fiber sampled at P5 shown in Figure 2a.

between the growth fronts of the kebabs G2 and G3, the two shishs are still left in a melt amorphous medium, and hence the subsequent overgrowth of kebabs occur from a double strands of shishs. The length l_D having the multiple strands of shishs may primarily depend on the growth rate of shishs relative to the propagation rate of the growth front of kebabs along the growth direction of shishs.

4.9. Shish-Kebab Formation: Memory Decay on Demixed Domains. Figure 12 is a typical TEM image at position P5 in the wound fiber shown in Figure 2a. It shows two shish-kebabs with interlocked lamellae having average lamellar thickness D and lamellar spacing L of 7.5 and 10 nm, respectively (Table 1). The memory of the domain boundaries is seen to almost disappear in the shish-kebabs. Such memory decay of the demixed domains occurs with an increasing degree in the order of images shown in Figure 11a1, Figure 11b1, and Figure 12. It is important to note that a whole space of the fiber at position P5 is filled with shish-kebabs and solvents molecules: the structures such as the demixed domains and the string-like structures having the domain memory were not observed. This simply suggests that all the structures observed in Figures 6−11 represent a series of transient structures developed in the kinetic pathway from homogeneous solutions to shish-kebabs.

5. DISCUSSION

5.1. Model for Structure Evolution along the Spinning Line: Universality Found in Self-assembled Dissipative Structures in Dynamically Asymmetric Systems. Figure 13 summarizes the results described in section 4 concerning the evolution of various dissipative structures (ordered structures developed in the open nonequilibrium systems) [part (b)] along the fiber spinning line [part (a)]. The kinetic pathway from entangled random coils swollen with solvent at P1 [as presented by Figure 6a1] to the well developed shish-kebabs swollen with solvent at P5 (Figure 12) comprises various transient self-assemblies as typically found at P2 to P4: the flow-induced plane-wave type concentration fluctuations at P2 which is driven by the stress-diffusion coupling [see the result shown in Figure 6b1]; oblate-ellipsoidal demixed domains with their revolution-axes oriented parallel to the flow direction and with their centers-of-mass aligned randomly in space at P3 (Figure 7); string-like self-assemblies of the demixed domains oriented parallel to the flow direction at P4−1 (Figure 8); string-like self-assemblies of densified demixed domains (Figure 9) with bundles of stretched chains parallel to the flow direction at P4−2 which are generated from the chains bridging the impinged demixed domains via CSCT [Figures 10, and 11(parts a1, a2)]. The uprise of $\Delta n(z)$ at least by a factor of ~3 occurred between the end of stage 1 at P4−1 and the end of stage 2 at P4−2 (Figure 5), corresponding to the crossover from the early stage to the late stage kinetic pathway shown in Figure 1D for the sheared solutions. The nucleation and growth of shishs and subsequent overgrowth of kebab lamellae from shishs occur between P4−2 and P5. Up to P4−1, chains in the demixed domains retain essentially randomly coiled conformation.

It should be noted here that the positions P4−1 and P4−2 are almost the same, both existing at $z \sim 100$ mm, although P4−1 exists slightly at an upstream side of P4−2. This reveals itself such an important fact that the transformation from stage 1 to stage 2 shown in Figure 13a occurs sharply over a small increase of the distance z at a given lateral position r, as will be defined in the last paragraph of this section in conjunction with Figure 13c, or over a small decrease of r at a given longitudinal position z, as will be also clarified later in this section.

The structure evolution found for the solutions of entangled UHMWPE/decalin along the fiber spinning line is complex, because it involves variations of temperature and strain rate. Nevertheless the structure evolution elucidated via the off-line snapshots of TEMs summarized in Figure 13 is strikingly similar to the isothermal time-evolution of the structures summarized in Figure 1 which are elucidated via the online snapshots of OMs, Δn, and SALS for both noncrystallizable solutions of entangled UHMWaPS/DOP and crystallizable solutions of entangled UHMWPE/paraffin under the shear flow fields generated by the cone-and-plate fixture. It is striking to note a remarkable universality found for these systems, with respect to the kinetic pathways and the specific self-assembled structures therein, by means of the off-line observations as summarized in Figure 13b and the online observations shown in Figure 1. The universality may well suggest that the model as summarized in Figure 13b constructed on the basis of the off-line observations essentially provide a good model expected for the structure evolution in the online fiber spinning process also. A common important physical factor responsible for the universality is the work done to these different systems by the applied flow fields under a maximum energy dissipation mechanisms.

It may be a big surprise at first glance to note the similarity of the shear flow effects and the extensional flow effects on these structure evolutions shown in Figure 1 and 13, since these two flow geometries are known to have different effects on molecular orientation and stress evolution. However we should note that the extensional flow field imposed on the fiber in the spinning line is complex, because the extensional strain rate and stress depend on the distance z from the spinneret along the spinning line, as expected from the z-dependence of Δn, the fiber diameter, temperature, etc. (see for example refs 48−50). It may be plausible that the extensional flow effects are still small at the positions P2, P3, and P4−1 closer to the spinneret, so that Δn and hence the chain orientation and stretching are negligibly small. This may explain why the transient structures evolved at P2, P3, and P4−1 are similar to those shown in Figure 1 under the step-up simple shear flow at given temperatures. The effects are expected to sharply increase with z beyond P4-2.

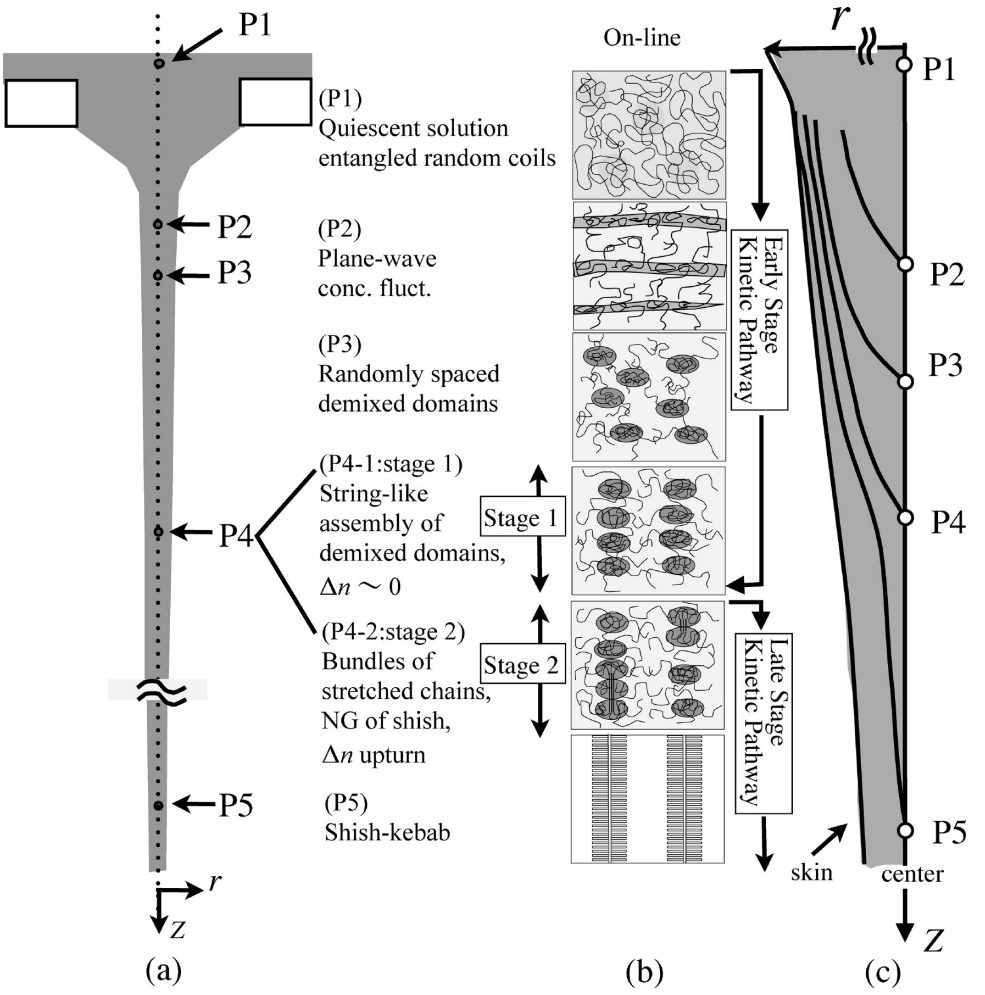

Figure 13. Summary of the dissipative structures evolved along the spinning line of the fiber spun from the UHMWPE solution: (a) schematic illustration of the fiber spinning and the sampling positions for the off-line TEM observations, (b) a proposed kinetic pathway from entangled random coils swollen with solvent at P1 to the shish-kebabs at P5, and (c) schematic illustration of contour lines representing the change in the transient structural transformation found along *z* with the lateral axis *r* of the fiber: the trajectory of each of the characteristic points P2 to P5 shifts upward with *r*, as schematically shown by the solid lines emanating from P2 to P5.

Finally, we should mention about the structure change with respect to the lateral direction, *r* as illustrated in Figure 13c. The structures evolved at P1 to P5 are found to shift toward upstream side with shifting observation line along the axis *r* from the center to the skin of the fiber (Figure 13c). This trend was confirmed by scanning TEM images along the lateral direction *r*, though the TEMs are not included in the manuscript. This shift is considered to be mainly due to the temperature gradient with respect to *r* with the cooling rate at the surface region of the fiber larger than that at the center region, hence the stress level being higher at the surface than at the center and the work done by flow increasing rapidly with *z* at the surface.

5.2. Shape of the Demixed Domains. As shown in Figure 7, the demixed domains have a shape of oblate ellipsoids with their revolution axes oriented statistically (on time- or ensemble-average) along the flow-direction. This reflects the history of the demixed domain formation, involving a transformation from the plane-wave type concentration fluctuations: when the amplitude of the plane-wave concentration fluctuations increases, the hydrodynamic interactions increase between the solvent flow and polymer chains in the regions rich in polymers; The solvent flow destabilizes the plane-wave concentration fluctuations and breaks them into the demixed domains having a more or less oblate ellipsoidal shape. This hypothesis about the transformation is experimentally supported by a TEM shown in Figure 14: Part a demonstrates the transformation process which generates partly thickened and thinned plane-wave concentration fluctuations as shown by the sketch with the white broken lines. Part b schematically presents the transformation mechanism. A thinner part b2, which is created in the polymer-rich region b1 driven by the solvent flow, becomes even thinner through the local capillary flow (indicated by the thin black arrows) driven by the capillary pressure; The thinner part is finally broken, creating the domains b3. Moreover, the transformation process can be also visualized by investigating the morphological variations along the lateral direction *r* from the center to the skin of the fiber as shown in Figure 14c, which shows simultaneously the region exhibiting the plane wave concentration fluctuations, the transient structures, and the demixed domains. It should be noted that Figures 14c and 6b1 are the TEMs taken near the surface region and the center core region of the same ultrathin section at P2, respectively. The unique orientation of the

dx.doi.org/10.1021/ma2008817 |*Macromolecules* 2011, 44, 7335–7350

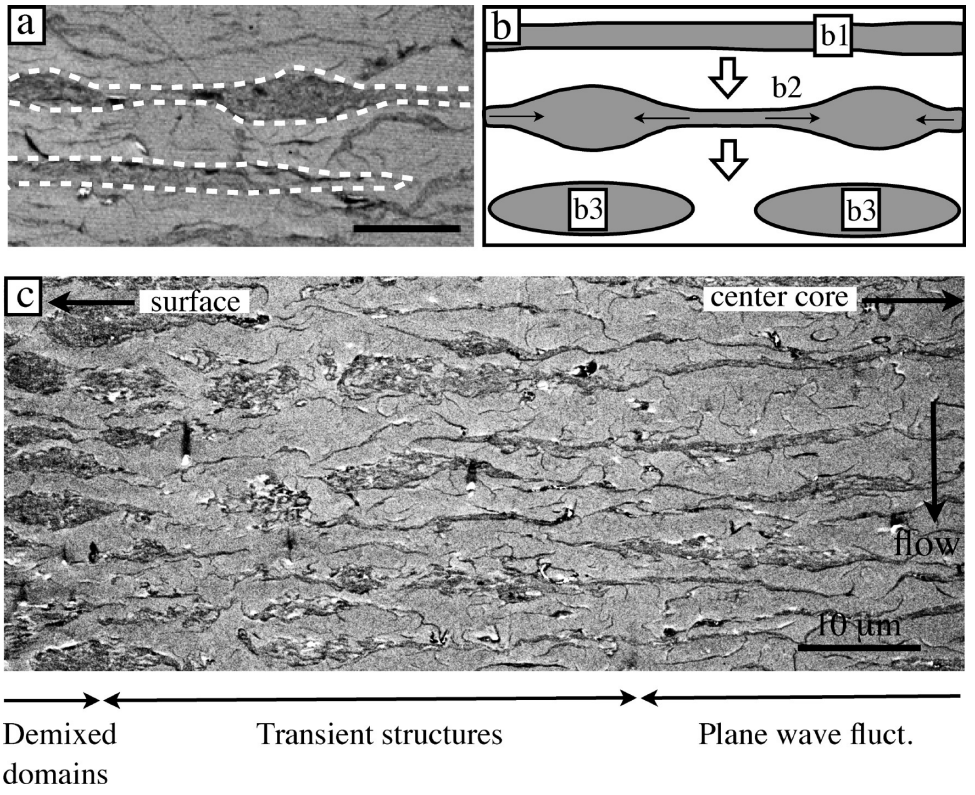

Figure 14. Transition from the plane-wave concentration fluctuations to the demixed domains: (a) TEM image showing transient structural transformation from the plane-wave fluctuations to the demixed domains; Partly thickened and thinned plane-wave concentration fluctuations are shown by the sketch with the white broken lines. (b) Schematic illustration of the transition, driven by the hydrodynamic effects, from the plane-wave concentration fluctuations to the demixed domains. (c) Continuous transition from the plane-wave concentration fluctuations to the demixed domains observed along the lateral direction from near the center to near the surface of the fiber.

demixed domains appears to be stabilized by existence of neighboring domains which interact each other.

5.3. Flow-Induced Alignment of Demixed Domains, Densification of Demixed Domains in the Strings, and Densification of the Strings in the Fibers: Trend toward Macro-Phase Separation. Figures 8−11 show an evolution of the string-like structures into a precursory structure of shish-kebabs at position P4−1 and P4−2. The hydrodynamic interactions between the solvent flow and the demixed domains align the demixed domains into the strings oriented parallel to the flow direction. The strings aligned parallel to flow themselves are aligned side by side laterally (along the direction perpendicular to flow), which gives rise to the nematic alignment of centers of mass of the demixed domains parallel to the flow direction. Moreover, the solvent flow causes off-aligned domains incorporate into the as-grown strings driven by the hydrodynamic interactions described above (Figure 9c), which leads the densification of the demixed domains in the strings, thereby giving rise to the solvent squeezing from the strings (Figure 9a). The strings themselves also are densified both laterally and longitudinally as shown in Figure 9b due to the hydrodynamic interactions between the solvent flow and the strings, resulting in the solvent squeezing out of the space between the string-like assemblies. The two kinds of the densifications, intra- and inter-string densification mediated by those hydrodynamic interactions, eventually lead to flow-induced growth of phase-separated structures toward macroscopic phase separation between the polymer-rich phase and the solvent-rich phase, flow-induced squeezing of solvents from the fiber and thereby the reduction of fiber diameters in the downstream of the fiber beyond the position P4. However, as-spun fiber at P5 in the wound bobbin still contains a lot of solvent, 30−50 wt % solvent.

5.4. Coil-to-Stretched Chain Transition Leading to Formation of Bundles of Stretched Chains and Nucleation- Growth of Shishs. We found out that the phase separation creates an excellent and rational field for polymer chains to crystallize into the shish-kebab morphology. In the new scenario, the demixed domains in the strings play two important roles: (1) The demixed domains impinged one another within the strings create bundles of stretched chains within the bridging domains formed at their domain boundaries where the local elongational strain rate imposed on polymer chains may be effectively enhanced and become larger than the bulk strain rate, then promote a growth of the bundles from the boundaries toward the interiors of the demixed domains, as evidenced by Figures 10 and 11, and eventually trigger the nucleation−growth of shishs within the bundles; (2) they serve as reservoirs for random coils which are efficiently transformed into kebab lamellae via the epitaxial crystallization from shishs.

Figure 15 shows a schematic model for the densification of the demixed domains in the string (a), formation of the bridging domains or bridging chains between the domains which are densified in the string (b), formation of bundles of stretched chains (c) and nucleation−growth of shishs within the bundles of stretched chains in the bridging domains at the boundaries of demixed domains (d), growth of the bundles of stretched chains

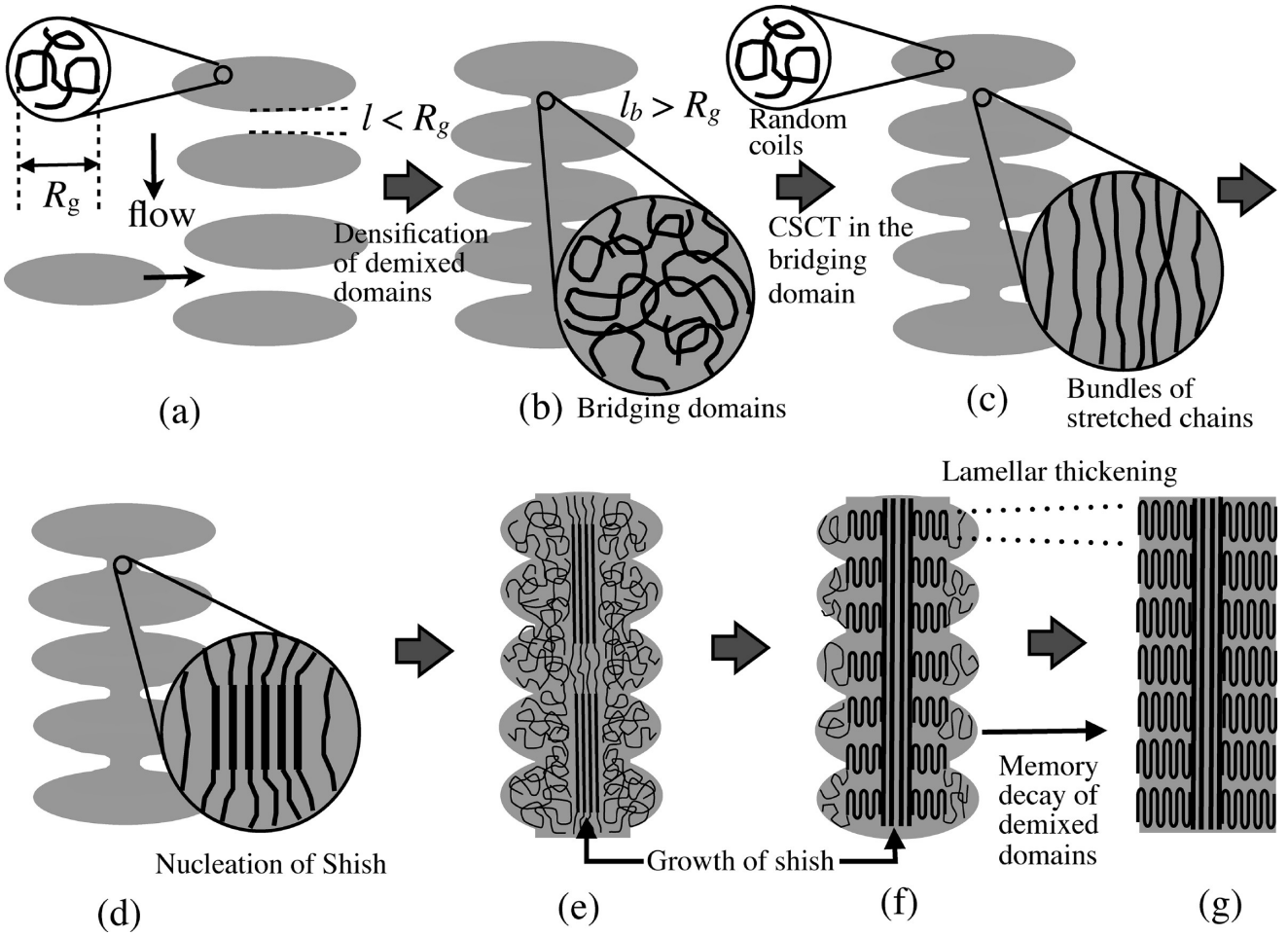

Figure 15. Schematic model showing transformation from the string to the shish-kebab: the densification of demixed domains in the string (a), formation of bridging domains or bridging chains between the domains densified in the strings (b), formation of bundles of stretched chains (c) and nucleation−growth of shishs in the bridging domains at the boundaries of the impinged demixed domains (d), growth of the bundles of the stretched chains and the shishs from the boundaries toward the interiors of the domains (e), and the epitaxial overgrowth of kebab lamellae from the random coils in the demixed domains onto the surface of the shish (f), and the long-range rearrangement of chain molecules within the as-grown shish-kebab which causes memory of the demixed domains within the shish-kebab decay to a more ordered shish-kebab (g).

and shishs from the boundaries to the interiors of the domains (e), and the epitaxial crystallization of the random coils in the demixed domains into kebab lamellae from shishs (f), and the long-range rearrangement of chain molecules within the as-grown shish-kebab, which causes the memory of the demixed domains within the shish-kebab decay to form a more ordered shish-kebab (g). The transformation from part a to part b is aimed to indicate the following two processes: (1) the densification of the demixed domains, which brings about the interstitial space between the neighboring domain interfaces at a distance l apart becomes smaller than R_g; (2) a part of the interstitial space is eventually transformed into the domain bridging the neighboring demixed domains with its length l_b along the string axis growing to become larger than R_g, the radius of gyration of chain molecules, via motions of the demixed domains mediated by the hydrodynamic interactions. The CSCT localized in the bridging domains (b) will cause formation of the bundles of stretched chains (c). From part e to part f, the growth of shishs dominantly occurs longitudinally but not laterally.[51] From part f to part g, long-range rearrangements of chains in the kebabs and shish leads to (i) lamellar thickening (Table 1) and (ii) a reduction of the average lateral size of the shish-kebabs,[51] and (iii) the decay of the memory of the demixed domains in the shish-kebabs.

In parts b and c of Figure 15, it may be puzzling why the chains or the domains bridging the demixed domains are under tension and why the chains inside the demixed domains are still in almost random coils. Although the generalization of the effect or expectation deserves future works, at this moment, we expect that: (i) the demixed domains are only partially draining or hardly draining with the solvent flow, hence the chains inside the demixed domains being kept essentially in random coils; (ii) motions of the demixed domains as a whole mediated by the solvent flow cause formation of the chains or domains bridging between the neighboring demixed domains; (iii) these bridging chains or bridging domains will be stretched again mediated by the solvent flow, which in turn cause bundles of stretched chains be formed within the bridging chains or domains via CSCT. It may be worth noting that the strain rate imposed on polymer chains in the bridging domains may be much larger than the bulk strain rate, which may promote the CSCT in the localized region.

We would like to propose the following model, as one of the plausible model, to explain the growth of the shish toward the

interior of the demixed domains which comprise essentially nondeformed entangled coils swollen with solvent as illustrated schematically in the change from Figure 15d to Figure 15e. The growth of the shish at a sufficiently large rate from the bundles of the stretched chains in the bridging domains (under the stress caused by the hydrodynamic interactions between the solvent flow and the densified demixed domains) causes the shish propagates toward the interior of the demixed domains according to the mechanism proposed by Petermann and Keller and co-workers,[52] which is based on the autocatalytic orientation of relaxed chains existing in front of the growing shish crystal chips.[53]

We conclude that the phase separation mediated by the stress-diffusion coupling inherent in the dynamic asymmetric component molecules provides a key for the kinetic pathway leading to shish-kebab formation. It is also important to note that the nature creates the shish-kebabs from entangled polymer solutions subjected to the flow via the *complex but rational* kinetic pathway as elucidated in this work. It should be also noted that the observation reported and the model presented here are restricted to homogeneous solutions of entangled polymers under a given spinning condition at this stage. However we have observed the similar trend on the kinetic pathway of the evolution of various transient dissipative structures at some different fiber spinning speeds for homogeneous solutions of the same UHMWPE with some different polymer concentrations involving the chain entanglements. Thus, we believe that the kinetic pathway observed here is universal, though the particular positions P1 to P4 along the spinning line, where the characteristic transitions in the self-assembly occur, will vary with the spinning speed and the polymer concentrations, because the transitions depend on the work done to the systems by the flow field.

The generalization of the observed effects and the proposed model on the polymer solutions to binary melt blends of UHMW and low molecular weight (LMW) polymers having the same monomeric units or to polymer melts having a large MW polydispersity deserve future works. Nevertheless we would like to stress again that the flow-induced phase separation is quite general for the dynamically asymmetric polymer systems (solutions or mixtures) having the large asymmetric parameter. In the binary melt blends of UHMW/LMW polymers, the LMW polymer and the UHMW polymer may be regarded as "solvent" and "polymer", respectively, in comparison to the case of polymer solutions. When the flow is imposed on the binary melts at temperatures higher than the nominal melting temperatures of the quiescent melts, the flow-induced phase separation is expected to occur between the "solvent" and "polymer" prior to the flow-induced crystallization and to play significant roles on the crystallization into the shish-kebab structure. We should note, however, a big difference between the binary melt blends and the polymer solutions in the following point: The "LMW solvent" in the binary melts can be incorporated in and cocrystallized with the shish and kebab crystals formed by the "UHMW polymer", though the solvent (paraffin or decalin) in polymer solutions can not be crystallized with the polymer.

5.5. Orientation of Lamellae Induced by Crystallization of Polymer Chains in a "Confined Space" Created by the Plane Wave Concentration Fluctuations or Demixed Domains. The lamellae in the specimens solidified at positions P2 and P3 are preferentially aligned with their normals parallel to the flow direction and hence perpendicular to the interface boundary of plane-wave concentration fluctuations or demixed domains with respect to the matrix solvent phase. Let us consider physical factors which cause the intriguing lamellae orientation found in the solidified sample at P2, which was described earlier in section 4.4 in conjunction with Figures 6b1 and 6b2, and at P3, which was described in section 4.5 in conjunction with Figure 7, parts b and c. The Δn developed at P2 and P3 was almost zero, hence the chains in the plane-wave concentration fluctuations and in the demixed domains remain essentially in random coils. The orientation of lamellae developed during the solidification process must not be caused by "conventional orientated crystallization", i.e., the crystallization induced by oriented chains, but be caused by the orientation induced by the demixed domain interfaces, i.e., the interface-induced lamellar orientation or by the orientation of the concentration fluctuations, i.e., the lateral growth of lamellae with their folded surfaces parallel to the isoconcentration surface which is normal to the flow.

6. CONCLUSIONS

In this work, we elucidated a kinetic pathway from entangled random coils swollen with solvent to shish-kebabs and a series of transient dissipative structures evolved therein along the fiber spinning line for concentrated UHMWPE solutions with the reduced concentration $c/c^* = 20$. The special sampling method of specimens from the fiber running through the spinning line and the special fixation methods of the specimens for TEM observations, as described in sections 3.3 and 3.4, respectively, enabled us to observe ex-situ the structures evolved online along the spinning line at the various positions, P1 to P5, which were solidified by the diffusion-limited crystallization occurring in the sampling method. We found that the kinetic pathway comprises the following two stages: the early stage and the late stage before and after the onset of the birefringence upturn, respectively, as summarized in Figure 13b.

In the early stage pathway, a series of various transient structures, typically represented by those at P2 to P4−1 in Figure 13b, are evolved from homogeneous solutions at P1 through the flow-induced phase separation. These transient structures developed by the phase separation have the characteristic length scale much larger than that covered by the conventional SAXS and SANS. In the late stage pathway, the flow-induced crystallization plays a dominant role on a further evolution of structures within the string-like structures developed via the flow-induced phase separation in the early stage pathway. Here in this stage, we expect an appearance of remarkable SAXS and SANS patterns in addition to the birefringence. The structure evolution in this stage is highlighted by the transformation of the structure at P4−2 to the one at P5 in Figure 13, and the mechanism underlying the structural evolution is schematically summarized in Figure 15c−g.

We propose that the coil-to-stretched chain transition (CSCT) occurs locally at the bridging domains (or chains) between the densified demixed domains in the strings [Figure 15b] to create the bundles of stretched chains there [Figure 15c]. Under the flow field involved in the spinning line, the bundles will further grow longitudinally (parallel to the flow-direction) from the boundaries toward the interiors of the demixed domains in the strings, followed by nucleation−growth of shishs and then the epitaxial crystallization of kebab lamellae onto shishs from the coils coexisting with a shish or shishs within the given string, as illustrated by a series of the models shown in parts d−f in Figure 15.

AUTHOR INFORMATION

Corresponding Authors

*E-mail: (H.M.) hiroki_murase@toyobo.jp; (T.H.) hashimoto@alloy.polym.kyoto-u.ac.jp.

Notes

[§]Honorary Chair Professor, National Tsing Hua University, Hsinchu, 30013, Taiwan

[⊥]Professor Emeritus, Kyoto University, Kyoto 606-8501, Japan

REFERENCES

(1) Mitsuhashi, S. *Bull. Text. Res. Inst. (J.)* **1963**, *66*, 1–9.

(2) Pennings, A. J.; Kiel, A. M. *Kolloid Z. Z. Polym.* **1965**, *205*, 160–162.

(3) Keller, A.; Kolnaar, H. W. H. In *Processing of polymer*; Meier, H. E. H., Ed.; VHC: New York, 1997; Vol. 18, Chapter 4.

(4) Meerveld, J. V.; Peters, G. W. M.; Hutter, M. *Rheol. Acta* **2004**, *44*, 119–134.

(5) Somani, R. H.; Yang, L.; Zhu, L.; Hsiao, B. S. *Polymer* **2005**, *46*, 8587–8623.

(6) Baert, J.; Puyvelde, P. V.; Langouche, F. *Macromolecules* **2006**, *39*, 9215–9222.

(7) Ogino, Y.; Fukushima, H.; Matsuba, G.; Takahashi, N.; Nishida, K.; Kanaya, T. *Polymer* **2006**, *47*, 5669–5677.

(8) Fernandez-Ballester, F. *Ph.D. Thesis*, California Institute of Technology, 2007.

(9) Kimata, S.; Sakurai, T.; Nozue, Y.; Kasahara, T.; Yamaguchi, N.; Karino, T.; Shibayama, M.; Kornfield, J. A. *Science* **2007**, *316*, 1014–1017.

(10) Kanaya, T.; Matsuba, G.; Ogino, Y.; Nishida, K.; Shimizu, H. M.; Shinohara, T.; Oku, T.; Suzuki, J.; Otomo, T. *Macromolecules* **2007**, *40*, 3650–3654.

(11) Mykhaylyk, O. O.; Chambon, P.; Graham, R. S.; Fairclough, J. P. A.; Olmsted, P. D.; Ryan, A. J. *Macromolecules* **2008**, *41*, 1901–1904.

(12) Balzano, L.; Rastogi, S.; Peters, W. M. *Macromolecules* **2009**, *42*, 2088–2092.

(13) Hayashi, Y.; Matsuba, G.; Zhao, Y.; Nishida, K.; Kanaya, T. *Polymer* **2009**, *50*, 2095–2103.

(14) Yan, T.; Zhao, B.; Cong, Y.; Fang, Y.; Cheng, S.; Li, L.; Pan, G.; Wang, Z.; Li, X.; Bian, F. *Macromolecules* **2010**, *43*, 602–605.

(15) Mykhaylyk, O. O.; Chambon, P.; Impradice, C.; Fairclough, J. P. A.; Terrill, N. J.; Ryan, A. J. *Macromolecules* **2010**, *43*, 2389–2405.

(16) Seki, M.; Thurman, D. W.; Oberhauser, J. P.; Kornfield, J. A. *Macromolecules* **2002**, *35*, 2583–2594.

(17) Hashimoto, T. *J. Polym. Sci., Part B: Polym. Phys.* **2004**, *42*, 3027–3062.

(18) Hashimoto, T. *Bull. Chem. Soc. Jpn.* **2005**, *78*, 1–39.

(19) Hashimoto, T. In *Soft Matter Characterization*; Borsali, R., Pecora, R., Eds.; Springer: Berlin, 2008; Chapter 8.

(20) Hashimoto, T.; Murase, H.; Ohta, Y. *Macromol. Sym.* **2009**, *279*, 88–95.

(21) Hashimoto, T.; Murase, H.; Ohta, Y. *Macromolecules* **2010**, *43*, 6542–6548.

(22) Doi, M.; Onuki, A. *J. Phys. II* **1992**, *2*, 1631.

(23) Onuki, A. *J. Non-Cryst. Solids* **1994**, *172*, 1151–1157.

(24) Helfand, E.; Fredrickson, G. H. *Phys. Rev. Lett.* **1989**, *62*, 2468–2471.

(25) Milner, S. T. *Phys. Rev. E* **1993**, *48*, 3674–3691.

(26) Onuki, A. *J. Phys., Condens. Matter* **1997**, *9*, 6119–6157.

(27) McHugh, A. J. In *Rheo-Physics of Multiphase Polymeric Systems*; Lyngaae-Jørgensen, J., Søndergaard, K., Ed.; Technomic Publishing: Lancaster, PA, 1995; Chapter 6.

(28) Murase, H.; Kume, T.; Hashimoto, T.; Ohta, Y. *Macromolecules* **2005**, *38*, 6656–6665.

(29) Murase, H.; Kume, T.; Hashimoto, T.; Ohta, Y. *Macromolecules* **2005**, *38*, 8719–8728.

(30) Murase, H.; Ohta, Y.; Hashimoto, T. *Polymer* **2009**, *50*, 4727–4736.

(31) de Gennes, P. G. *J. Phys. Chem.* **1974**, *60*, 5030–5042.

(32) Dukovski, I.; Muthukumar, M. *J. Chem. Phys.* **2003**, *118* (14), 6648–6655.

(33) Muthukumar, M. *Adv. Polym. Sci.* **2005**, *191*, 241–274.

(34) Wang, M. *J. Phys. Chem. B.* **2010**, *114*, 3488–3493.

(35) Ver Strate, G.; Phillipoff, W. *J. Polym. Sci., Polym. Lett.* **1974**, *12*, 267.

(36) Yanase, H.; Moldenaers, P.; Mewis, J.; Abetz, V.; van Egmond, J.; Fuller, G. G. *Rheol. Acta* **1991**, *30*, 89.

(37) Hashimoto, T.; Fujioka, K. *J. Phys. Soc. Jpn.* **1991**, *60*, 356–359.

(38) Hashimoto, T.; Kume, T. *J. Phys. Soc., Jpn.* **1992**, *61*, 1839–1843.

(39) Wu, X.-L.; Pine, D. J.; Dixon, P. K. *Phys. Rev. Lett.* **1991**, *66*, 2408–2411.

(40) Saito, S.; Hashimoto, T.; Morfin, I.; Lindner, P.; Boue, F. *Macromolecules* **2002**, *35*, 445–459.

(41) Murase, H.; Kume, T.; Hashimoto, T.; Ohta, Y.; Mizukami, T. *Macromolecules* **1995**, *28*, 7724–7729.

(42) Endoh, M. K.; Takenaka, M.; Inoue, T.; Watanabe, H.; Hashimoto, T. *J. Chem. Phys.* **2008**, *128*, 164911–1−164911−12.

(43) Kume, T.; Hattori, T.; Hashimoto, T. *Macromolecules* **1997**, *30*, 427–434.

(44) Saito, S.; Takenaka, M.; Toyoda, N.; Hashimoto, T. *Macromolecules* **2001**, *34*, 6461–6473.

(45) Matsuzaka, K.; Hashimoto, T. *Rev. Sci. Instrum.* **1999**, *70*, 2387–2397.

(46) Brandrup, J., Immergut, E. H., Grulke, E. A., Eds. *Polymer Handbook*; 4th ed.; John Wiley & Sons. Inc.: New York, 1999.

(47) Riddick, J. A.; Bunger, W.; Sakano, T. K. *Organic Solvents*; 4th ed.; John Wiley & Sons. Inc.: New York, 1986.

(48) Katayama, K.; Amano, T.; Nakamura, K. *Kolloid-Z. Z. Polym.* **1968**, *226*, 125–134.

(49) Kim, K. H.; Cho, H. H.; Ito, H.; Kikutani, T. *J. Polym. Sci., Part B: Polym. Phys.* **2008**, *46*, 847–856.

(50) Kase, S. *J. Appl. Polym. Sci.* **1974**, *18*, 3267–3278.

(51) Ohta, Y.; Murase, H.; Hashimoto, T. *J. Polym. Sci., Part B: Polym. Phys.* **2010**, *48* (17), 1861–1872.

(52) Lieberwirth, I.; Loos, J.; Petermann, J.; Keller, A. *J. Polym. Sci., Part B: Polym. Phys.* **2000**, *38*, 1183–1187.

(53) Note added in proof. The growing shish crystal chip is expected to keep creating a bundle of mesomorphically ordered chains in front of its growing chip, defined here as the "mesophase front" having size l and w parallel and perpendicular to the chain direction, within the demixed domains which are composed of almost nondeformed coils, according to the mechanism proposed by Petermann-Keller and co-workers[52]. In order to keep the longitudinal growth (growth parallel to the chain direction) of the crystal into shish in the mesophase front, the mesophase front may have to satisfy a specific condition about w and l, e.g., $w/l > (w/l)c$ where $(w/l)c$ is a critical value of w/l; Otherwise the lateral growth of the crystal may happen to occur within the mesophase front.[54]

(54) Strobl, G. *Eur. Phys. J. E* **2000**, *3*, 165–183.